Three-Dimensional Structure of the Gap Junction Connexon

Guy Perkins,* Dan Goodenough,# and Gina Sosinsky*§
Departments of *Neurosciences and §Biology, University of California, San Diego, La Jolla, California 92093-0322, and #Department of Cell Biology, Harvard Medical School, Boston, Massachusetts 02115 USA

ABSTRACT The gap junction membrane channel is composed of macular aggregations of intercellular channels permitting the direct intercellular transfer of ions and small molecules. Each intercellular channel is formed by the apposition of two hexameric transmembrane channels (connexons), one from each cell. The interlocking of the two channels occurs extracellularly in a narrow 3.5-nm "gap" separating the junctional membranes. The channel-channel interaction is known to be selective between members of the family of proteins, called connexins, which oligomerize into the connexons. In addition to selectivity, the molecular interfaces involved in the extracellular interactions between connexons must be very congruent, since the intercellular channel must provide high resistances to the leakage of small ions between the channel lumen and the extracellular space. By using a recently developed biochemical procedure for obtaining ordered arrays of connexons from gap junctions split in the extracellular gap, (Ghoshroy, S., D. A. Goodenough, and G. E. Sosinsky. 1995. Preparation, characterization, and structure of half gap junctional layers split with urea and EGTA. *J. Membr. Biol.* 146:15–28) a three-dimensional reconstruction of a connexon has been obtained by electron crystallographic methods. This reconstruction emphasizes the structural asymmetry between the extracellular and cytoplasmic domains and assigns lobed structural features to the extracellular domains of the connexon. The implication of our hemichannel structure is discussed in relation to the in vivo state of unpaired connexons, which have been shown to exist in the plasma membrane.

INTRODUCTION

Intercellular communication through gap junction channels has functional roles in cell survival, differentiation, metabolism, morphogenesis, and mutagenesis (Bennett et al., 1991; Dermietzel et al., 1990; Fraser et al., 1987; Gilula et al., 1972; Goodenough et al., 1996; Hooper and Subak-Sharpe, 1981; Revel et al., 1985). Gap junctions are specialized cell-cell contact regions that contain tens to thousands of intercellular channels that link two apposed cells. These channels facilitate a form of intercellular communication by permitting the regulated passage of ions and small molecules from one cell to another (Bennett and Goodenough, 1978).

Gap junction intercellular channels are composed of two paired transmembrane protein oligomers (connexons), one from each juxtaposed membrane. Each connexon contains six homomeric or heteromeric subunits made from members of a multigene family of homologous proteins called connexins (Beyer et al., 1990; Jiang and Goodenough, 1996; Makowski et al., 1977; Sosinsky, 1995; Stauffer, 1995). The channel-channel interaction is known to be selective between connexins. In addition to selectivity, the molecular interfaces involved in the extracellular interactions between connexons must be congruent, since the intercellular channel must provide high resistances to the leakage of small ions between the channel lumen and the extracellular space. The connexin proteins are designated by the abbreviation Cx followed by the molecular mass in kilodaltons, e.g., rat Cx32 is the predominant connexin found in rat liver connexons.

Proteolysis and antibody binding experiments indicate that the family of connexins have a common folding topology with the peptide chain traversing the membrane four times (Beyer et al., 1987; Goodenough et al., 1988; Hertzberg et al., 1988; Milks et al., 1988; Nicholson et al., 1985; Yancy et al., 1989; Zhang and Nicholson, 1989; Zimmer et al., 1987). The N- and C-termini are located on the cytoplasmic side of the junctional membrane, while the extracellular (or "gap") side of the membrane contains two loops, called E1 and E2. Comparisons of the amino acid sequences of known connexins have shown that while the amino terminus, the four membrane spanning domains, and the two extracellular loops are relatively conserved, the remainder of the cytoplasmic domains are highly variable. (White et al., 1995).

Several lines of evidence imply that the connexon structure at the cytoplasmic surface is disordered (Sosinsky, 1992). The cytoplasmic structure has not been adequately visualized in either the three-dimensional reconstructions from electron microscopy (Sikerwar et al., 1991; Sikerwar and Unwin, 1988; Unwin and Ennis, 1984; Unwin and Zampighi, 1980) or in x-ray diffraction analyses (Makowski et al., 1984; Tibbitts et al., 1990). Fourier averages of images of cardiac gap junctions containing Cx43 at ~16 Å resolution are almost identical in projection with liver gap junctions (Yeager and Gilula, 1992) in spite of ~11-kDa mass difference between Cx43 and Cx32 in the C-terminal tail. Endogenous proteolysis of Cx43 produces a connexin that is missing an ~13-kDa fragment but the Fourier averages of images of the proteolyzed samples are almost identical to the unproteolyzed specimens. Removal of the cyto

Received for publication 28 May 1996 and in final form 16 October 1996.
Address reprint requests to Dr. Guy Perkins, NCMIR, University of California, San Diego, La Jolla, CA 92093-0608. Tel.: 619-534-7968; Fax: 619-534-7497; E-mail: perkins@ncmir.ucsd.edu.

0006-3495/97/02/533/12 $2.00

plasmic domains from liver gap junctions by proteolysis also does not significantly change the high-resolution equatorial reflections in x-ray diffraction patterns, although the mass loss was visualized in the electron density profiles calculated from x-ray diffraction meridional data (Makowski et al., 1984).

In contrast, the transmembrane and extracellular domains of the connexons are more highly ordered in isolated gap junction specimens, and thus are amenable to Fourier analyses. Modeling studies, CD spectra, and analyses of high-angle x-ray diffraction data are consistent with α-helical secondary structure in these ordered domains (Cascio et al. 1990, 1995; Milks et al., 1988; Tibbitts et al., 1990; Unwin, 1986). The model that best fits the x-ray diffraction data contains a four α-helical bundle with one or two of the helices tilted ~20° with respect to the membrane plane. Analysis of meridional arcs centered at 4.9 Å that are sampled by an ~80-Å interference function locates the α-helical scattering centers in the transmembrane domains; however, the data are not of sufficient resolution to permit the dissection of specific contributions of each putative helix from contributions of the extracellular domains (Tibbitts et al., 1990).

The involvement of the connexin extracellular domain in cell-cell interaction has been studied using several approaches. Biochemically, the E1 and E2 loops each contain three conserved cysteines, and Dahl et al. (1991, 1992) have shown that mutation of any of these six cysteine residues in Cx32 completely blocks the development of gap junctional conductances between *Xenopus* oocyte pairs. Site-specific E1 and E2 antisera will stearically interfere with gap junction assembly between certain cells in culture (Meyer et al., 1992). White et al. (1994) showed that the E2 domain is a determinant of connexin selectivity in heterotypic connexon interactions. Foote and Nicholson (1997) moved the first and third cysteines of each E-loop of Cx32 to various positions away from their wild-type positions. Only if the Cys residues are moved in pairs, such that their relative positions permit continued disulfide bonding, will functional channels result. The least perturbation of channel-forming capacity and biophysical properties are observed if the Cys residues are moved precisely two residues in either direction, consistent with a β-sheet secondary structure. Further experiments by Foote and Nicholson suggest a model in which the extracellular domains form stacked β-sheets, each with a central reverse turn, which are joined and held in a rigid conformation by three interloop disulfide bonds.

Due to the extremely tight interlocking of the connexons in the extracellular gap necessary for ionic insulation of the intercellular channel pore, images of the extracellular domains of the connexons are difficult to obtain from intact intercellular channels at low resolution. Current connexon models, therefore, are based on reconstructions of the entire channel, which is then divided at the midpoint to produce a single connexon (for example, see Unwin and Zampighi, 1980). Topographic images of the extracellular surfaces have been obtained by atomic force microscopy (AFM), which show distinct lattice structure and some subunit detail, and indicate a rigidity to the extracellular structure sufficient to resist the mechanical dissection performed by the AFM cantilever (Hoh et al., 1991, 1993). The rigidity of the extracellular domain is in agreement with the x-ray data and evidence for disulfide-bonded β-sheets reviewed above.

While connexons are known to be present in the nonjunctional membranes of cultured cells (Musil and Goodenough, 1991), they are not clustered in sufficient density to permit a structural analysis. Ghoshroy et al. (1995) refined a protocol developed by Manjunath et al. (1984) for reproducibly obtaining single connexon layers or "split junctions" with high efficiency and good structural integrity. A good example of a split junction is shown in Fig. 1 *A*. These split junctions offer the opportunity to visualize the extracellular surface of the connexon. The specimens have permitted a three-dimensional reconstruction of connexons formed from Cx32 and Cx26 from rat liver at a resolution of ~20 Å by the technique of 3-D electron crystallography. From this reconstruction, new information about the topology of the extracellular domain was determined.

MATERIALS AND METHODS

Isolation and splitting of gap junctions

Preparations of isolated gap junctions were made from rat liver using a detergent extraction procedure, which is detailed in Fallon and Goodenough (1981) and Baker et al. (1985). Purified plaques of gap junctions were split with urea and EGTA as described by Ghoshroy et al. (1995). SDS-PAGE of both intact and split gap junctions was performed (Goodenough et al., 1988) to check that proteolysis was minimal.

Electron microscopy

Split gap junctions were adsorbed to carbon-coated grids rendered hydrophilic by UV light and stained with 2% uranyl acetate. Low-dose, cryo-EM images were taken at a nominal magnification of 35,000 on a Philips CM12 electron microscope, operated at 120 kV, and equipped with a Gatan 651 anticontaminator and a Gatan 626 cold stage cooled to ~−175°C. Tilting of the specimens to provide three-dimensional (3-D) data was achieved with a goniometer stage. Tilt series with tilts up to 62° and tilt angle increment of either 10 or 20° within each series were collected. The defocus was ~450 nm (as measured by optical diffraction) which resulted in the first zero in the phase contrast transfer function (PCTF) lying beyond the 16-Å resolution cutoff used in the 3-D reconstruction. Tilt series quality was assessed both visually and by optical diffraction. Tilt series of split gap junction patches were rejected if they did not diffract to at least 20 Å resolution. Typically, these images had distinctly visible connexons. Five tilt series (41 images) satisfied the resolution criteria and provided an adequate sampling of Fourier space.

Image analysis

Fourier methods (Henderson et al., 1986) were used to generate the 3-D reconstruction of the gap junction connexon. Micrographs were digitized on an Eikonics CCD model 1412 microdensitometer at a raster of 20 μm (5.7-Å pixel size). The image area that provided the best optical diffraction was further reduced after digitization to optimize the strength of the structure factor amplitudes determined from the computed diffraction pattern. This area was computer-processed as shown in the flow chart

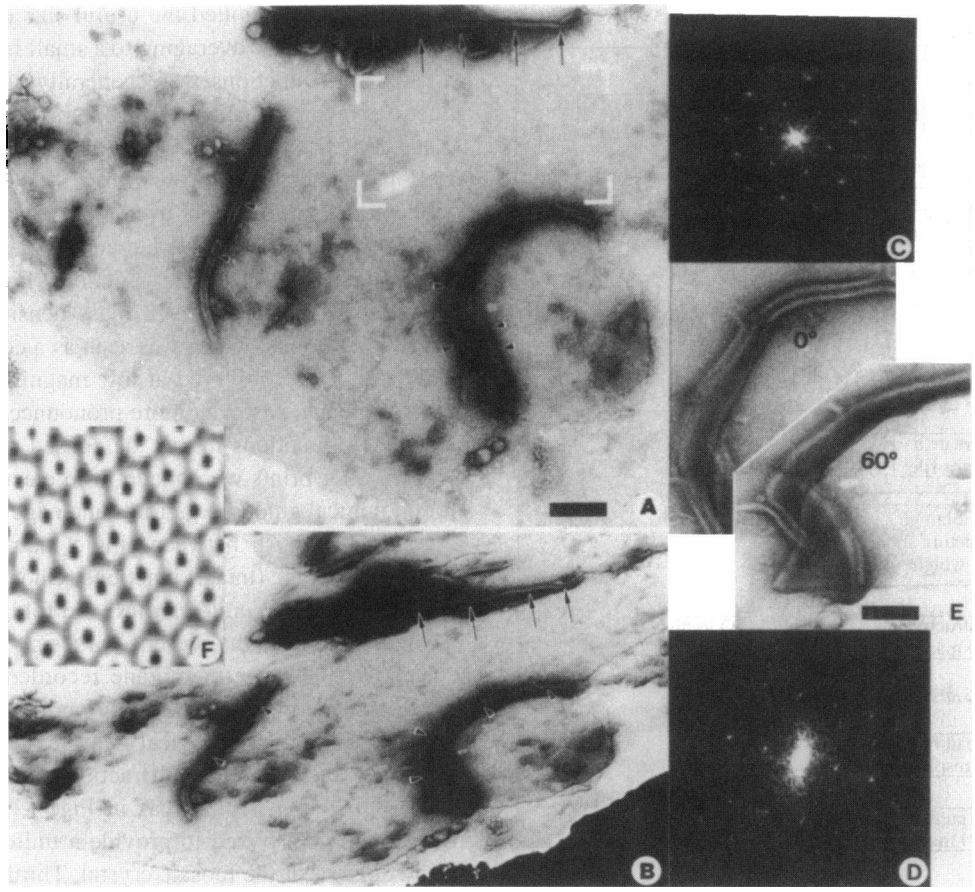

FIGURE 1 Electron micrographs recorded at ~−175°C and 120 kV of split gap junctions stained with uranyl acetate. (*A*) Untilted image of split plaques. Curled edges (*arrows*) and folds (*arrowheads*) confirm the presence of single membranes. Individual connexons are visible on a hexagonal lattice and appear as "doughnuts." The digitized area is boxed. (*B*) Image of the same membrane recorded at 60° tilt. Scale bar = 150 nm. (*C*) Computed diffraction pattern, after crystal lattice unbending, from an image area in (*A*) that was boxed to provide a uniform lattice. The lattice constant is 83 Å. Third-order reflections are clearly visible and higher-order reflections can be detected above the background after image processing. (*D*) Same as (*C*) but computed from a boxed image taken from the 60° image of (*B*). (*E*) Magnified subareas of (*A*) and (*B*) providing details of the edge views of hemichannel membranes at 0° and 60° tilts. Scale bar = 61 nm. (*F*) Filtered image generated by masking the reflections of the computed diffraction pattern of (*C*) with a six-pixel radius circular filter, and then computing the inverse Fourier transform. A smaller region of ~6 × 6 connexons is shown. The pore (*dark circle* at the center of each connexon) is an outstanding feature. The region between connexons, the lipid bilayer, is also darker than the connexon protein mass, but not as dark as the pore.

provided in Fig. 2. A combination of software packages was used to take advantage of the unique capabilities of each. The majority of programs used were from the MRC Electron Microscopy (Crowther et al., 1996) and CCP4 (Collaborative Computational Project 4, 1994) packages. Crystal lattice distortions were corrected by the methods described by Henderson et al. (1986) using the SPECTRA software package (Schmid et al., 1993). Each image was brought to a common phase origin by the program ORIGTILT. The structure factor phases were close to 0 or 180° for the nominally untilted images. Hence the plane group symmetry must be centrosymmetric (e.g., p2, p6). The program ALLSPACE further confirmed p6 symmetry for 2-D crystals of connexons. The expected resolution in projection was estimated by the program AVRGAMPHS and extends to ~15 Å.

Calculation and display of 3-D maps

The nominally untilted image data were first combined. Images were subsequently merged in order of increasing tilt. Merging was performed using the crystallographic plane group, p6, since it was previously determined that split gap junctions from liver maintain the hexagonal substructure found in intact gap junctions (Ghoshroy et al., 1995). The tilt angles and axes were calculated by the Shaw and Hills (1981) procedure. The 3-D merging of structure factors (Amos et al., 1982) was accomplished with ORIGTILT using p6 symmetry. The 3-D data set contained 37 of 41 images that could be merged with low phase residuals. The program LATLINE (Agard, 1983) was used to fit smooth curves along each reciprocal lattice line. The merged images, ranging in tilt angles from −60° to +62°, sampled the lattice lines sufficiently to follow the continuous variations in amplitudes and phases. Sampling the curves at intervals of 0.005 $Å^{-1}$ provided the amplitudes and phases used for calculating the 3-D connexon map. The effect of the PCTF on the structure factor amplitudes was corrected. The program PREPMKMTZ converted LATLINE output into the mtz format used by the suite of CCP4 programs and removed unreliable phase measurements. The CCP4 programs were used to calculate the 3-D map using Fourier terms sampled along the lattice lines at intervals of 0.005 $Å^{-1}$. Figure-of-merit (FOM) weighting was used to downweight unreliable structure factors. Also, a B-factor of −5000 $Å^2$ was employed to ameliorate the unreasonably high scaling of low-resolution amplitudes obtained by the PCTF correction. Contour plots of map sections were generated using PLUTO. The surface-rendered maps were displayed

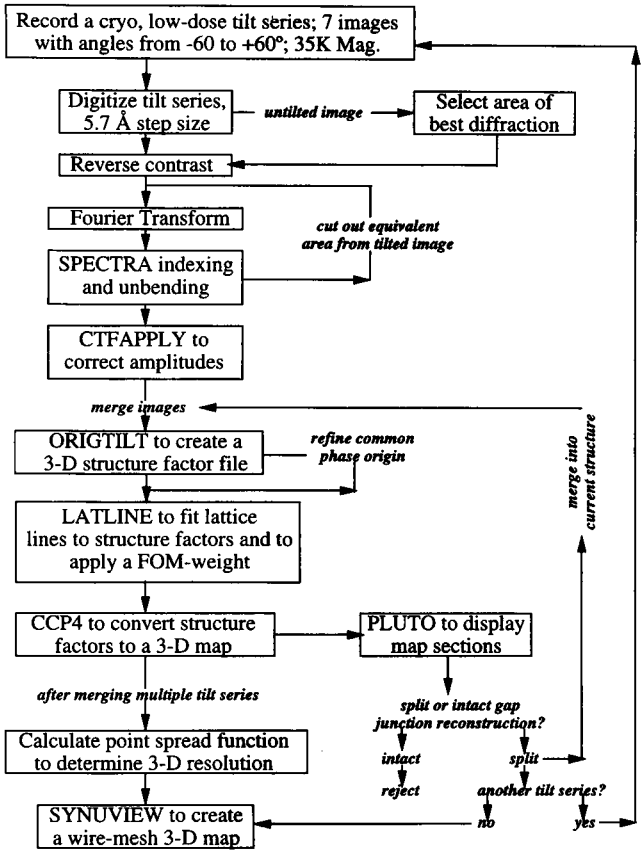

FIGURE 2 Flow chart describing the computer processing of electron micrographs (see Experimental Procedures for a description of the image processing). The name of the program used at each step in the flow chart is capitalized. Note that a 3-D reconstruction was computed from each tilt series, which allowed differentiation of split gap junction membranes from intact membranes.

with the SYNU graphics package (Hessler et al., 1992). The molecular envelope of the connexon was estimated by the program DALTON, and confirmed by the program SYNUVOLUME. The point spread function (PSF) (Born and Wolf, 1980; Stevens et al., 1994) was calculated to estimate the 3-D resolution for our 3-D map using the method described by Unger and Schertler (1995).

RESULTS

Specimen characterization

A low-irradiation image of an untilted gap junction plaque that had been chemically split using the protocol developed by Ghoshroy et al. (1995) is shown in Fig. 1 *A*. The contrast in this image was quite good, as indicated by the visibility of the connexon lattice in the original micrograph. The effect of the urea and EGTA used in this splitting protocol was the separation of the two connexon membranes while maintaining the structural integrity of the connexon lattice. The two-dimensional, hexagonal lattice observed after splitting had the same lattice constant and packing arrangement found in the whole junctions. As with intact junction crystals, connexon crystals displayed a relatively high degree of mosaicity, which limited the useful size of a coherent area for crystallographic averaging to a small fraction of the total plaque. Split junctions were generally smaller than intact junctions, which may have been the result of fracturing along domain boundaries of the mosaic crystals, as previously postulated (Ghoshroy et al., 1995).

There are three criteria, used at various stages before the final 3-D map was generated, that were used to differentiate between split and intact gap junctions. First, at the microscopy stage, the difference in mass density between intact and split junctions, which was seen as a contrast difference, could usually be observed at low magnification. This contrast difference was even more pronounced when searching for suitable junctions in the "defocused diffraction mode." Second, after prints were made from electron micrographs, morphological guides, e.g., folds and edge appearance, were used to distinguish between single membrane (split) and double membrane (intact) junctions (Ghoshroy et al., 1995). The curled edges (*single arrows*) and folds (*double arrows*) in Fig. 1 *A* indicate the presence of a single membrane. Fig. 1 *B* shows the same membrane recorded at 60° tilt. This high-tilt image provides even more pronounced edge views confirming the morphological guides of Fig. 1 *A*. Fig. 1, *C* and *D* are the computed diffraction patterns, after crystal lattice unbending, from areas in Fig. 1, *A* and *B*, respectively, that were boxed to provide a uniform lattice, i.e., a single domain of the mosaic crystal. Third-order reflections were clearly visible, and fourth-order reflections were detected above the background after image processing. In the third criterion for single membranes, a 3-D reconstruction was calculated from each of the five tilt series used in the final 3-D connexon map. Although a reconstruction computed from only seven images is low-resolution, this was sufficient to confirm that these membranes were indeed single connexon layers.

To detect stain penetration inside the lipid bilayer that may have resulted from detergent extraction of lipid or from the urea extraction procedure, we a) present magnified edge views and b) generated a filtered image. Fig. 1 *E* shows views looking down the edge of the membrane tilted 0° and 60°. If significant stain penetration had occurred, then the membrane would appear darker in the edge view than in the perpendicular view through the stain-excluding (connexon) mass. The edge view of the hemichannel membrane does indeed appear darker, but not to the extent that we can unequivocally assert that stain significantly penetrated the bilayer. The filtered image, generated by masking the reflections of the computed diffraction pattern with a 6-pixel radius circular filter, is shown in Fig. 1 *F*. Filtering eliminated noise from the image and resulted in a sharper view of the connexons. The darker regions between connexons might indicate stain penetration. However, it is equally likely that these regions indicate disordered areas, e.g., noncrystalline lipid packing, that were lost upon local averaging.

Improvement in image quality

Multiple passes of crystal lattice unbending provided a much greater number of reflections above the noise level in computed diffraction patterns. Correcting for long-range, translational lattice distortions resulted in a two to threefold increase in the signal-to-noise ratio (S/N) of summed intensities. Fig. 3 shows boxes of intensities summed around the expected reflection position for all reflections in two resolution ranges from the diffraction pattern of Fig. 1 *C*. This figure indicates that a relatively strong signal was present beyond a resolution of 25 Å. The low-resolution summed intensity (83—25 Å) was many times higher than the medium-resolution summed intensity (25—20 Å) because negative stain preservation greatly enhanced the strength of low-resolution intensities. Below 20-Å resolution, the summed intensities dropped to ~2 times the background. The first pass of lattice unbending provided a map showing areas of good cross-correlation between the reference area (3 × 3 unit cells cut out from the image center) and the entire image area. Only those areas showing good cross-correlation peaks were subsequently boxed for a second pass of lattice unbending. We found that boxing around only the most coherent areas significantly improved the S/N, usually by 30–50%, after unbending.

Scaled intensities (83 Å - 25 Å resolution)

8	9	5	8	10	7	8	5	5
11	6	6	13	16	7	5	7	7
9	9	11	15	29	18	11	10	5
17	7	11	114	313	92	9	14	9
16	7	24	305	1028	324	32	26	14
14	10	16	44	128	59	7	14	6
11	9	9	19	42	26	13	21	5
11	15	8	16	17	15	9	10	7
17	13	14	14	11	8	9	9	11

Scaled intensities (25 Å - 20 Å resolution)

5	6	5	10	15	10	7	11	10
4	3	5	8	7	3	6	5	14
7	17	11	8	4	8	4	9	4
12	6	5	10	5	4	11	5	5
6	11	6	20	36	9	10	10	8
6	19	25	33	40	11	5	3	5
8	7	3	8	5	5	3	3	6
9	12	9	13	5	10	5	5	3
9	8	8	8	12	9	15	5	4

FIGURE 3 Summed intensities in boxes around expected reflection positions after crystal lattice unbending. Reflections from the diffraction pattern of Fig. 1 *C* were separated into two resolution ranges, low (83–25 Å) and medium (25–20 Å).

Assessment of image and 3-D reconstruction quality

Each of the five tilt series was used to create separate 3-D reconstructions and confirmed that only images of single membranes were merged into the final map. Structure factor amplitudes and phases varied continuously perpendicular to the plane of the connexon membrane, giving continuous lattice lines along z^*. Merging images with different tilts provided values of the amplitudes and phases at different sections through the reciprocal lattice lines. Table 1 provides merging statistics for images in four tilt ranges. The number of common spots between an image to be merged with the previously merged images must be sufficiently high such that the phase origin will be brought to the p6 phase origin, in common with all merged images. Even in the highest tilt range there was a sufficient number of common reflections to unambiguously merge each added image to the common phase origin. Phase residuals were based on comparisons between each added phase and all previously accumulated values related by symmetry. The low phase residuals (~13-18°) presented in Table 1 were due in part to the inclusion of only the strongest reflections, but also reflected the accuracy of the determined lattice and tilt parameters. These low residuals also indicated that the error in merging was minimal.

Fig. 4 shows lattice lines for the six strongest reflections. The phase data possessed a small degree of scatter, indicating reliability of features in the 3-D map produced from these data. To ameliorate the artificial boost in low-resolution amplitudes caused by correcting for the PCTF and to correct for the dominance of overly strong low-resolution amplitudes produced by negative-stain embedment (see Fig. 2) a scale (temperature) factor was used to boost the medium-resolution amplitudes (Unger and Schertler, 1995) and is plotted in Fig. 4. A criterion used to select a proper temperature factor was that it should not change which reflection had the largest amplitude relative to the rest of the data. For our data, the reflection with the largest amplitude was the [1,0,0]. When the temperature factor magnitude was 7000 $Å^2$ and above, the reflection with the largest amplitude was no longer the [1,0,0], but rather a much higher-resolution reflection, which indicated that this value was too high. Another criterion for selecting a proper temperature factor

TABLE 1 Merging statistics as a function of image tilt angle

Range of tilt angles	Number of Images	Common reflections for merging*	Phase residual#
0–5°	5	18.2	13.2°
5–25°	12	17.0	17.7°
25–45°	11	13.2	17.8°
45–65°	9	8.2	13.8°

*The mean number of independent reflections from a newly merged image in common with previously merged images, using only IQ 1–5 spots. Z^* bin of 0.005 $Å^{-1}$.

#The mean phase residual from a newly merged image compared with previously merged images, using the common reflections.

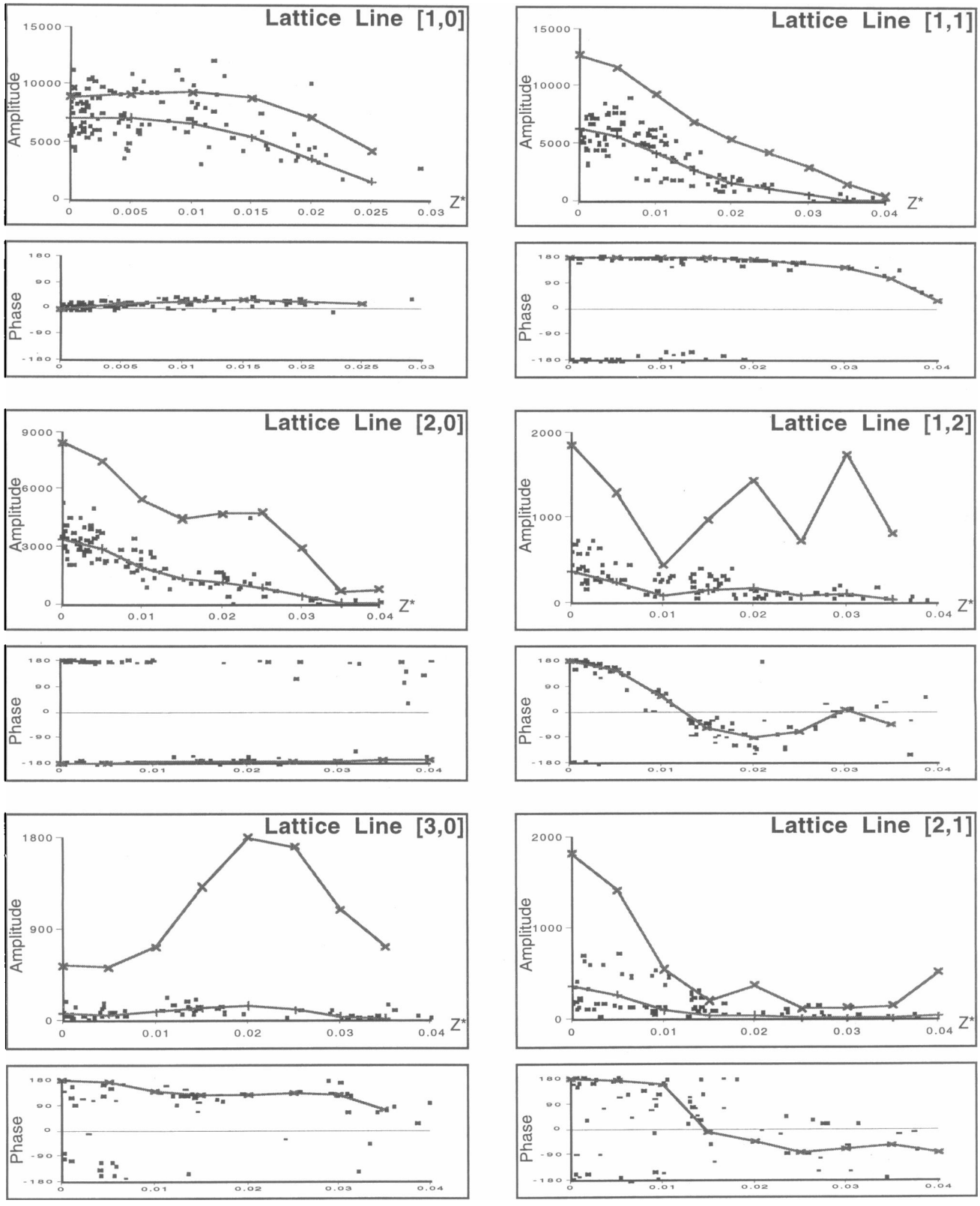

FIGURE 4 Structure factor amplitudes (*top*) and phases (*bottom*) for a few representative lattice lines (*hk*) are plotted versus z^*. The phases are constrained by plane group symmetry (p6) to have phases of 0° or 180° only at $z^* = 0.0$. The program LATLINE fits a curve to the data points based on p6 symmetry constraints. Amplitudes and phases were subsequently read from the curve at equal intervals, represented by crosses. Plots of the LATLINE curves after applying a temperature factor of $B = -5000$ Å^2 show the scaling performed before generating the 3-D map, represented by X. Temperature factors with magnitudes below 5000 Å^2 did not significantly enhance the features of the unscaled map, while factors above this value introduced artifacts in the map. The result of temperature factor scaling was to sharpen the appearance of features that could already be detected in the unscaled map.

was the appearance of the map itself. A value of 7000 $Å^2$ or more produced what appeared to be artifacts in the connexon boundary, which were eliminated when a value of 5000 $Å^2$ was used. The effect of this scaling was to provide a more detailed map representing the true resolution contained in the merged data.

3-D connexon map and the reliability of structural features

The 3-D reconstruction of the gap junction connexon emphasized the asymmetry between the extracellular and the cytoplasmic domains (Fig. 5, *A—D*). The cytoplasmic and extracellular surfaces of the maps were assigned based on three lines of evidence. First, the feature at the threefold axis was previously determined to lie on the cytoplasmic surface based upon the distance it moved between tilted and untilted images of the same negatively stained intact junctions (Baker and Sosinsky, unpublished results). Second, trypsin treatment of these same specimens (only the cytoplasmic domains were enzyme-accessible) removed the feature at the threefold axis and replaced it with a pocket of stain that also had the same distance constraints. Third, the six protrusions, assigned to the extracellular surface, have also been seen in AFM images of the extracellular surface (Hoh et al., 1993).

The map shown in Fig. 5 was contoured at 90% and 80% of the theoretical volume. The observed features remained strong even at a display level of 65% of the theoretical volume. If all parts of the Cx32 were visible, the cytoplasmic domains would contribute ~47%, the extracellular domains ~26%, and the transmembrane domains ~27%, respectively, to the volume. However, these values are only approximations based on current topological models of the primary sequence (Goodenough et al., 1988). An 81% volume would correspond to a connexon composed solely of Cx26 connexons. Cx32 and Cx26 are found in a 10:1 ratio, respectively, in isolated rat liver gap junctions (Zhang and Nicholson, 1989). However, at this resolution, Cx32, Cx26, and Cx32/Cx26 heteromeric connexons are indistinguishable.

While the extracellular surface had well-defined features (Fig. 5 *D*), the cytoplasmic side was relatively flat (Fig. 5 *C*), apparently because of peptide flexibility in this region, which was viewed as disorder in the crystallographic approach used (reviewed by Sosinsky, 1992, 1996). Hence, the height of the connexon seen was only ~50 Å, as depicted in the central section (Fig. 5 *B*) perpendicular to the membrane. This height correlated well with the expected

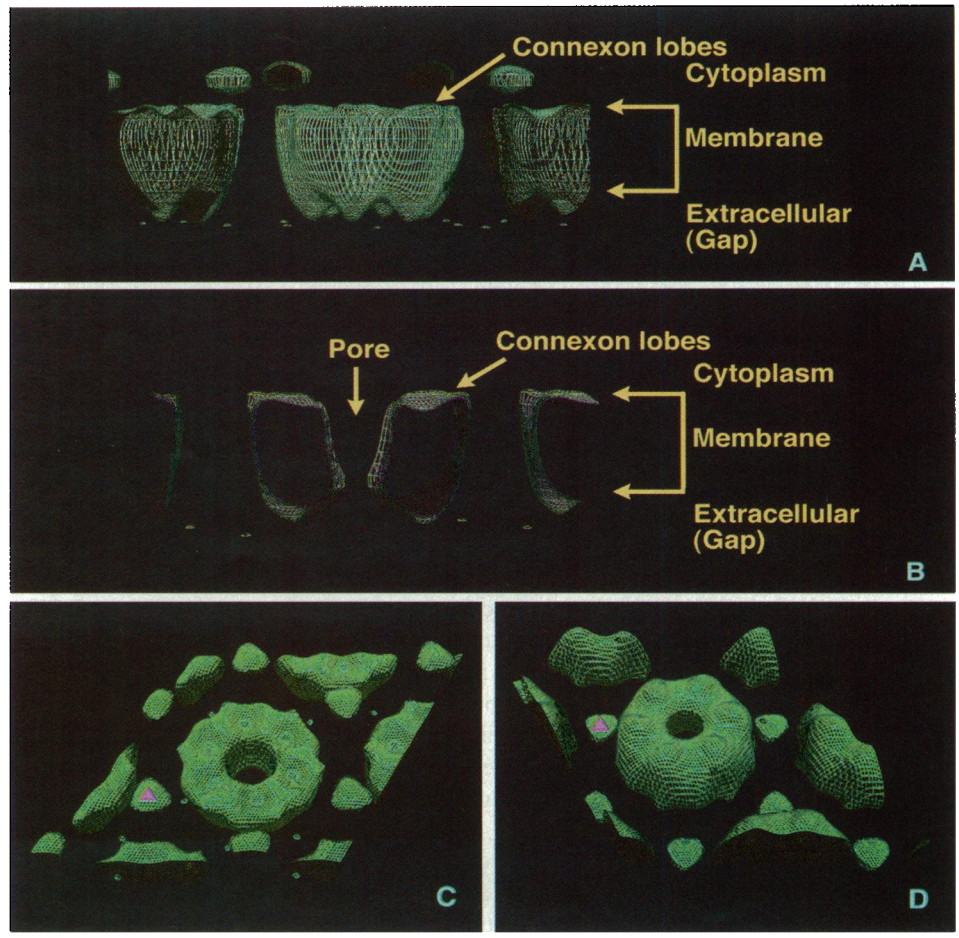

FIGURE 5 Complementary views of the connexon map. Shown here is the p6 unit cell with a central connexon and parts of the surrounding connexons at the edges of the unit cell. (*A*) A side view of the entire map showing the asymmetry of the cytoplasmic and extracellular side. The contours are at 90% (*yellow*) and 80% (*blue*) of the theoretical volume. There are six lobes that protrude from the extracellular surface. In contrast, the cytoplasmic side shows little height modulation. (*B*) shows a view of the central portion (16-Å thick) cut parallel to the *x*-axis and emphasizes how the channel tapers toward the extracellular side. (*C*) A view looking down the cytoplasmic portion of the structure, at a small angle from the sixfold axis. The triangle denotes the threefold axis where stain-excluding mass is observed. The thickness of the connexon is 50 Å. (*D*) Connexon reconstruction viewed looking down the extracellular side at a small angle from the sixfold axis, located at the center of the connexon.

membrane width of ~35-40 Å (Makowski et al., 1977; Tibbitts et al., 1990) plus the measured extracellular height of 14 Å (Hoh et al., 1993). The distance that each connexon protruded into the gap is ~15 Å, in good agreement with one-half the gap width of negatively stained cross sections of intact junctions from grid sections (~30 Å thick, Sosinsky et al., 1988). The shrinkage due to the electron beam and stain drying was reduced by the combination of low temperature (−175°C) and a low number of images in each tilt series (Sikerwar et al., 1991; Sikerwar and Unwin, 1988; Sosinsky et al., 1988). Initial trial experiments showed that a seven-image exposure series made no discernible difference in image quality between the first and last exposures, as judged by computed diffraction intensities.

To obtain information about the topology at the extracellular domains, an estimate of the connexon molecular envelope was determined. Physiological, biochemical, and structural results indicate that living organisms assemble channels containing different connexins (Jiang and Goodenough, 1996; Sosinsky, 1995; Stauffer, 1995). It has been hypothesized that plaques with the best crystalline order are selective for homomeric channels (all six connexins in a connexon of the same type) or heterotypic channels (each connexon composed of a different type of connexin) whereas loosely packed maculae are selective for heteromeric channels (different types of connexins in a single connexon, Harris, 1997; Sosinsky, 1996). Since the connexon layers used in the reconstruction showed good crystalline order, it was assumed that homomeric connexons were present. Therefore, the molecular volume was estimated to be 241,000 $Å^3$ based on the connexon molecular mass of ~192,000 kDa. Since it is known that portions of the cytoplasmic domains are disordered, this molecular volume was an overestimate of the protein density. This volume was then used to contour the density in Fig. 5 to display the molecular envelope. A pore ran all the way through the center of the connexon and was constricted to a diameter of ~16 Å on the extracellular end. The connexon had a diameter of ~65 Å and the six density peaks protruding up from the extracellular face were presumed to be the portions of the six connexon subunits that would dock with an apposing connexon to form an intercellular channel. The open pore on the extracellular end and the six density protrusions were also observed in atomic force microscope (AFM) images of mechanically dissected connexons (Hoh et al., 1993). Prominent stain-excluding density was also observed at the threefold axis of the unit cell on the cytoplasmic surface (Fig. 5, *A* and *C*) which has been reported in the literature (Baker et al. 1983, 1985; Caspar et al., 1988). This feature has been absent in other published 3-D reconstructions of the double membrane structure. Since this density was discontinuous with the main connexon body (density center is ~10 Å from the closest edge of the connexon) it was unclear what this feature might represent.

Contour plots of sections parallel to the membrane at the cytoplasmic edge and the extracellular surface are shown in Fig. 6, *A* and *B*, respectively. These sections provided a

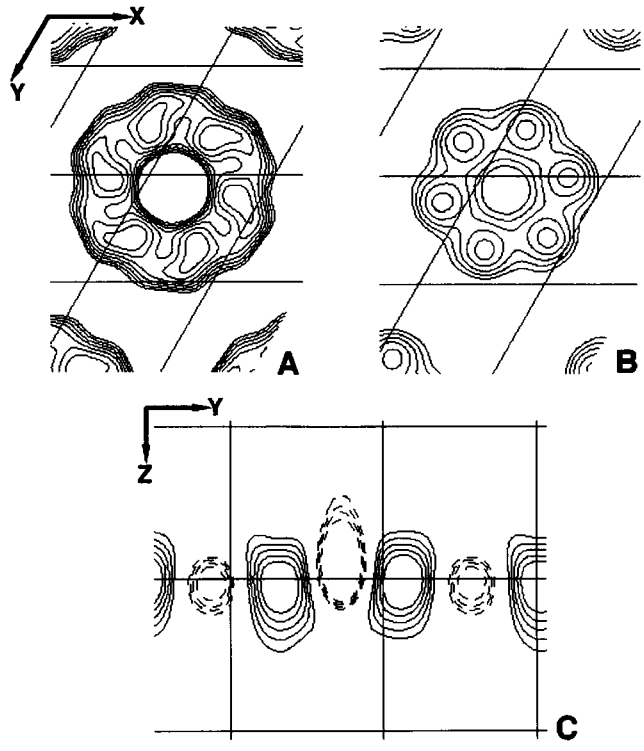

FIGURE 6 Contour plots of 5-Å sections cut from the 3-D map. (*A*) Section parallel to the membrane plane at a level corresponding to the cytoplasmic edge and (*B*) the extracellular edge of the connexon. (*C*) Central section perpendicular to the membrane plane through the pore. Solid contours represent positive density, i.e., stain-excluding regions (ordered protein) and dashed contours represent negative density, i.e., regions of stain accumulation or nonordered regions.

perspective not easily seen in Fig. 5 *C* and showed the hexagonality and skewing similar to the Baker et al. (1983) projections. These sections also showed a similar twist of the subunits between the cytoplasmic and extracellular sides, as was seen by Unwin and co-workers (Unwin and Zampighi, 1980; Unwin and Ennis, 1984). Fig. 6 *C* is a contour plot viewing the reconstructed connexon perpendicular to the pore, hence perpendicular to the contour plots of Fig. 6, *A* and *B*. Negative contours are shown to investigate the possibility that sufficient lipid was removed in the detergent extraction or perhaps during the urea-EGTA splitting procedure such that stain had penetrated in the region between connexons. High concentrations of urea (8 M) have been used to solubilize the platelet glycoprotein complex IIb.IIIA, an integral membrane protein (Gianazza et al., 1992). Because the negative contours between connexons are nearly as strong as those in the pore, stain penetration between connexons might have occurred. However, crystallographic averaging provides a reconstruction of only those areas that are ordered. Thus, an alternative explanation is that the negative contours represent disordered mass (cf. Fig. 1 *F*).

The effective resolution of the 3-D map was estimated from the point spread function (PSF, Fig. 7) of the input

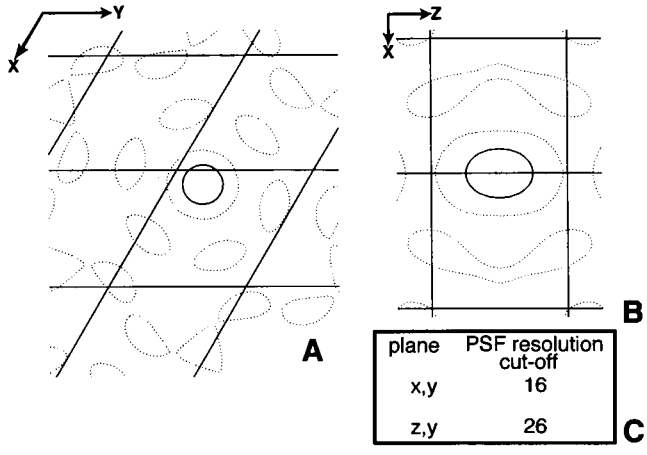

FIGURE 7 Sections (x, y) and (x, z) through the point spread function of the experimental 3-D data. Solid contour lines are at the peak half-height and the dotted contour lines are at the zero level. The underlying gridlines have a spacing of 40 Å. The resolution cutoffs, as measured from these plots, are given to the side.

data (described by Unger and Schertler, 1995). The PSF was used as a measure of the anisotropic resolution. The PSF-calculated resolution cutoffs were ~16 Å in plane and ~26 Å perpendicular to the membrane plane. The reduced resolution in the vertical direction was due to incomplete 3-D sampling; since the highest tilt angle was 62°, there was an unsampled wedge of Fourier space. As a check of feature reliability, a comparison of an uncorrected ("raw") map and the final PCTF/B factor-corrected map showed that the overall features in each were similar (data not shown).

DISCUSSION

The data gathered from electron micrographs of split gap junctions have permitted a three-dimensional reconstruction of a single connexon. Previous reconstructions were obtained from the double membrane structure and a single connexon was estimated by simply dividing the structure down the center of the extracellular space (Sikerwar and Unwin, 1988; Unwin and Ennis, 1984; Unwin and Zampighi, 1980). The reconstruction shown here provides a visualization of the topology at the extracellular surface avoiding an arbitrary separation of the paired connexons in the extracellular space.

The key to obtaining the single connexon reconstruction was the development of a reproducible procedure for splitting isolated gap junctions with high efficiency, resulting in connexon plaques of good structural integrity (Ghoshroy et al., 1995). Previous protocols for splitting the membrane pair produced variable and partial splitting and/or disordered membrane structure. By using a combination of urea, chelating agents, and temperature, >75% split junctions could be obtained that also maintained a hexagonal crystal lattice.

Relevance of uncoupled connexons to isolated connexons in vivo

Our hemichannel structure is relevant to the increasing interest shown in the mechanism of hemichannel assembly before reaching the plasma membrane, aggregation in the plasma membrane, and finally docking with a hemichannel from an adjacent cell. The oligomerization of connexins into a connexon (reviewed by Laird, 1996) is atypical of integral membrane proteins in that it occurs in the *trans*-Golgi network (Musil and Goodenough, 1993) instead of taking place in the endoplasmic reticulum (Hurtley and Helenius, 1989). Laird postulates that oligomerization occurs in such a "late" compartment because "earlier" secretory compartments may be unable to prevent connexon pairing. There is also the expectation that hemichannels in the *trans*-Golgi network are closed to maintain the integrity of the Golgi membrane. Biochemical studies have provided evidence that unpaired connexons exist in the plasma membrane (DeVries and Schwartz, 1992; Evans, 1994; Musil and Goodenough, 1993). In addition, evidence for the presence of functional hemichannels was obtained from expression of rat Cx46, chick Cx56, bovine Cx44, and *Xenopus* Cx38 in single *Xenopus* oocytes. In these studies, channels form in the nonjunctional plasma membrane and open on depolarization (Paul et al., 1991; Ebihara and Steiner, 1993; Ebihara et al., 1995; Gupta et al., 1994, Ebihara, 1996).

Comparison with other structural data

Similar to previous reconstructions from intact gap junctions (Sikerwar and Unwin, 1988; Unwin and Ennis, 1984; Unwin and Zampighi, 1980) the single connexon reconstruction showed an open pore in the connexon center running completely through the membrane. It was possible that the pore was closed within the cytoplasmic domain (not well-visualized in this reconstruction) which may control gating (Makowski, 1988). While no major substructure was visible at the cytoplasmic surfaces, slight modulations of surface structure were seen that were distinctly different from the classic skewed-lobe appearance (compare Fig. 5 *C* and Fig. 6 *A*). It was possible that some of the surface modulation seen on the cytoplasmic side may have been due to contributions from the cytoplasmic loop or base of the carboxy tail from each of the six connexin molecules. The hexagonal substructure of the connexon was readily apparent (even before imposing sixfold symmetry). An additional common feature was the slight tapering of the molecular envelope at the extracellular end when viewed parallel to the membrane plane (best seen in cross section; Fig. 5 *B*). Since we do not have an accurate estimate of the membrane boundaries, this tapering may lie just outside of the lipid bilayer at the extracellular surface.

Unlike previous reconstructions from intact gap junctions (Unwin and Ennis, 1984; Unwin and Zampighi, 1980), the connexon pore tapered from the cytoplasmic end to the extracellular end. A broader cytoplasmic opening is consis-

tent with sucrose accessibility measurements on the pore (Makowski et al., 1984). The pore had a narrowest diameter of ~16 Å, although this measurement was at the resolution limit in the map. Given the considerable experimental manipulation required for the isolation and splitting of the gap junctions, the two extracellular loops (per connexin) may have experienced rearrangements that resulted in the appearance of a constriction. Nevertheless, the connexon structure remained highly hexagonal after splitting and maintained the ~8° skew from vertical, as previously observed by Baker et al. (1983, 1985) and Gogol and Unwin (1988).

It is interesting to note that we see continuous density through the membrane in our map. While this result was unexpected based on the current dogma of negative staining, it is not unique. Karlsson et al. (1983) and Böttcher et al. (1992) also reported 3-D maps of membrane proteins, cytochrome reductase, and photosystem I (PS I), respectively, obtained from negatively stained crystals that showed strong density through the membrane. In both structures, the highest densities were those in the transmembrane region. We present three hypotheses for our observations. The first two explanations we have mentioned previously in the paper, i.e., stain penetration through the membrane due to the biochemical manipulation of the sample or loss of features in the lipid regions due to the crystallographic averaging process. Stain penetration into a crevasse in the bilayer between protein and surrounding lipids, formed by electron irradiation, is a possibility in view of a new 3-D reconstruction of PS I (Karrasch et al., 1996). While their structure also shows densities within the membrane, there is weaker contrast through the membrane than in the same area of the 3-D reconstruction of Böttcher et al. (1992). Karrasch et al. (1996) attributed this lower contrast to using a much lower electron dose. Stain penetration into crevasses as a result of electron irradiation were first described by Unwin and Klug for tobacco mosaic virus (1974). However, the appearance of cross-sectional views through our membranes, fortuitously obtained by folds or membrane edges, do not show significant stain darkening. A third proposal is that contributions from the transmembrane domains are being seen as a result of the stability of the specimen at low temperature. In essence, at low temperature, the negative stain may act as a mold to hold the protein in place, allowing enhanced crystallographic averaging. A similar explanation has been proposed in spot-scan images where the unirradiated areas hold irradiated spots in place (Downing, 1991). Rachel et al. (1986) and Valpuesta et al. (1990) have reported high-resolution images from negatively stained specimens. At higher resolution, these images contain contributions from the protein as well as the stain. In principle, if the structural preservation is good, then the images obtained should be the sum of the stain and protein.

AFM images of mechanically split gap junction plaques (Hoh et al., 1991, 1993) possess both similar and dissimilar features to the 3-D connexon reconstruction. An opening at the extracellular surface and little structural detail at the cytoplasmic surface are common features. Other features in common include the protrusions (height modulations) rising above the membrane on the extracellular side, which may indicate that the contact surface between connexons in apposing membranes is not flat. Hoh et al. (1993) suggested that two connexons may dock in the same fashion as intermeshing cogs. This hypothesis requires that apposing connexons be rotated 30° with respect to each other such that the peaks on one connexon fit into the valleys of the other connexon. Given the ionically tight interface created between connexons in the assembled intercellular channel, it seems unlikely that the connexons interact at the tips of the protrusions, as this would result in a palisade of molecular gaps corresponding to the aligned valleys at the connexon/connexon interface. Our hemichannel structure presents tantalizing evidence for the intermeshing cogs model of connexon-connexon interaction.

One important dissimilarity between the 3-D map and the AFM images was the channel pore diameter. AFM images provide a channel pore diameter of 38 Å at the extracellular side, which is about twice the diameter (~16 Å) in the connexon reconstruction. Hoh et al. (1993) offered an explanation that the AFM tip might have pushed out certain parts of the protein, causing an artificial broadening of the channel pore.

Connexin secondary structure in the connexon

The x-ray diffraction analysis by Tibbitts et al. (1990) indicated that there was more α-helical content than could be accounted for by four transmembrane helices. The E1 and E2 loops are thought to be as rigid as the transmembrane domain (Hoh et al., 1993; Sosinsky, 1992). Hence, the extracellular region is visible with the crystallographic averaging used. Each extracellular protrusion may therefore include an extension of the intramembrane α-helical structure (Tibbitts et al., 1990). As reviewed in the introduction, mutagenesis studies have suggested that the extracellular loops contain disulfide-bonded β-sheet conformation (Foote and Nicholson, 1997), which would be expected to act as a rigid domain. Even though the transmembrane structure has not been implicated in determining the compatibility of docking connexons, it may contribute to the structure of the channel wall in the gap region of the channel. However, it is possible that the occurrence of a conformational change upon junctional splitting may give rise to the observed sixfold protrusions seen in both chemically split or mechanically split junctions (Hoh et al., 1993).

It is known that hydrogen bonding plays a substantive role in connexon pairing because urea is required to biochemically split connexon pairs (Manjunath et al., 1984; Ghoshroy et al., 1995). The percentage of hydrophobic amino acids in the E2 loop is high, and so hydrophobic interactions are involved in the extracellular connexon pairing. Ghoshroy et al. (1995) also provide evidence that divalent cations contribute to stabilizing the docking of

apposing connexons. The availability of a 3-D reconstruction of this key appositional interface will permit modeling of the protein-protein interactions involved in the cell-cell interactions at gap junctional connexon interfaces.

We express our appreciation to Mark Ellisman for the use of his excellent facilities. We are grateful for the programs and advice given by Terry Frey, Stephan Lamont, David Morgan, and Vinzenz Unger.

This work was funded by National Institutes of Health Grants GM43217 (to G.E.S.) and GM18974 (to D.A.G.). Some of the work included here was conducted at the National Center for Microscopy and Imaging Research at San Diego, which is supported by National Institutes of Health Grant RR04050 to Mark H. Ellisman.

REFERENCES

Agard, D. A. 1983. A least-squares method for determining structure factors in three-dimensional tilted-view reconstructions. *J. Mol. Biol.* 167:849–852.

Amos, L. A., R. Henderson, and P. N. T. Unwin. 1982. Three-dimensional structure determination by electron microscopy of two-dimensional crystals. *Prog. Biophys. Mol. Biol.* 39:183–231.

Baker, T. S., D. L. D. Caspar, C. J. Hollingshead, and D. A. Goodenough. 1983. Gap junction structures. IV. Asymmetric features revealed by low-irradiation microscopy. *J. Cell Biol.* 96:204–216.

Baker, T. S., G. E. Sosinsky, D. L. D. Caspar, C. Gall, and D. A. Goodenough. 1985. Gap junction structures VII. Analysis of connexon images obtained with cationic and anionic negative stains. *J. Mol. Biol.* 184:81–98.

Bennett, M. V. L., L. C. Barrio, T. A. Bargiello, D. C. Spray, E. Hertzberg, and J. C. Saez. 1991. Gap junctions: new tools, new answers, new questions. *Neuron.* 6:305–320.

Bennett, M. V. L., and D. A. Goodenough. 1978. Gap junctions, electronic coupling, and intercellular communications. *Neurosci. Res. Prog. Bull.* 16:375–486.

Beyer, E. C., D. L. Paul, and D. A. Goodenough. 1987. Connexin43: a protein from rat heart homologous to a gap junction protein from liver. *J. Cell Biol.* 105:2621–2629.

Beyer, E. C., D. L. Paul, and D. A. Goodenough. 1990. Connexin family of gap junction proteins. *J. Membr. Biol.* 116:187–194.

Born, M., and E. Wolf. 1980. Principles of Optics. Pergamon Press, Oxford.

Böttcher, B., P. Graber, and E. J. Boekema. 1992. The structure of photosystem I from the thermophilic cyanobacterium *Synechococcus* sp. determined by electron microsopy of two-dimensional crystals. *Biochim. Biophys. Acta.* 1100:125–136.

Cascio, M., E. Gogol, and B. A. Wallace. 1990. The secondary structure of gap junctions. Influence of isolation methods and proteolysis. *J. Biol. Chem.* 265:2358–2364.

Cascio, M., N. M. Kumar, R. Safarik, and N. B. Gilula. 1995. Physical characterization of gap junction membrane connexons (hemi-channels) isolated from rat liver. *J. Biol. Chem.* 270:18643–18648.

Caspar, D. L. D., G. E. Sosinsky, T. T. Tibbitts, W. C. Phillips, and D. A. Goodenough. 1988. Gap junction structure. *In* Gap Junctions. E. L. Hertzberg and R. G. Johnson, editors. Alan R. Liss, Inc., New York. 117–133.

Collaborative Computational Project 4. 1994. The CCP4 suite: programs for protein crystallography. *Acta Crystallogr. D.* 50:760–763.

Crowther, R. A., R. Henderson, and J. M. Smith. 1996. MRC image processing programs. *J. Struct. Biol.* 116:9–16.

Dahl, G., E. Levine, C. Rabadan-Diehl, and R. Werner. 1991. Cell/cell channel formation involves disulfide exchange. *Eur. J. Biochem.* 197: 141–144.

Dahl, G., R. Werner, E. Levine, and C. Rabadan-Diehl. 1992. Mutational analysis of gap junction formation. *Biophys. J. (Discussions)* 62: 187–195.

Dermietzel, R., T. K. Hwang, and D. S. Spray. 1990. The gap junction family: structure, function, and chemistry. *Anat. Embryol.* 182:517–528.

DeVries, S. H., and E. A. Schwartz. 1992. Hemi-gap-junction channels in solitary horizontal cells of the catfish retina. *J. Physiol.* 445:201–230.

Downing, K. H. 1991. Spot-scan imaging in transmission electron microscopy. *Science.* 251:53–59.

Ebihara, L. 1996. *Xenopus* connexin38 forms hemi-gap-junctional channels in the nonjunctional plasma membrane of *Xenopus* oocytes. *Biophys. J.* 71:742–748.

Ebihara, L., V. M. Berthoud, and E. C. Beyer. 1995. Distinct behavior of connexin56 and connexin46 gap junctional channels can be predicted from the behavior of their hemi-gap-junctional channels. *Biophys. J.* 68:1796–1803.

Ebihara, L., and E. Steiner. 1993. Properties of a nonjunctional current expressed from a rat connexin46 cDNA in *Xenopus* oocytes. *J. Gen. Physiol.* 102:59–74.

Evans, W. H. 1994. Assembly of gap junction intercellular communication channels. *Biochem. Soc. Trans.* 22:788–792.

Fallon, R. F., and D. A. Goodenough. 1981. Five-hour half-life of mouse liver gap junction protein. *J. Cell Biol.* 90:521–526.

Foote, C. I., and B. J. Nicholson. 1997. Determination of disulfide bond patterns in the extracellular docking domains of gap junctions. *J. Cell Biol.,* submitted.

Fraser, S. E., C. R. Green, H. R. Bode, and N. B. Gilula. 1987. Selective disruption of gap junctional communication interferes with a patterning process in hydra. *Science.* 237:49–55.

Ghoshroy, S., D. A. Goodenough, G. E. and Sosinsky. 1995. Preparation, characterization, and structure of half gap junctional layers split with urea and EGTA. *J. Membr. Biol.* 146:15–28.

Gianazza, E., R. Frattini, S. Michelagnoli, M. Cassinotti, and C. R. Sirtori. 1992. Isoelectric focusing and immunoblotting of the platelet membrane glycoprotein complex IIb. IIIA following urea solubilization. *Electrophoresis.* 13:781–784.

Gilula, N. B., O. R. Reeves, and A. Steinbach. 1972. Metabolic coupling, ionic coupling, and cell contacts. *Nature.* 235:262–265.

Gogol, E., and N. Unwin. 1988. Organization of connexons in isolated rat liver gap junctions. *Biophys. J.* 54:105–112.

Goodenough, D. A., J. A. Goliger, and D. L. Paul. 1996. Connexins, connexons, and intercellular communication. *Annu. Rev. Biochem.* 65: 475–502.

Goodenough, D. A., D. L. Paul, and L. Jesaitis. 1988. Topological distribution of two connexin32 antigenic sites in intact and split rodent hepatocyte gap junctions. *J. Cell Biol.* 107:1817–1824.

Gupta, V. K., V. M. Berthoud, N. Atal, J. A. Jarillo, L. C. Barrio, and E. C. Beyer. 1994. Bovine connexin44, a lens gap junction protein: molecular cloning, immunological characterization, and functional expression. *Invest. Ophthalamol. & Visual Sci.* 35:3747–3758.

Harris, A. 1997. Connexin structure/function. *Quart. Rev. Biophys.,* in preparation.

Henderson, R., J. M. Baldwin, K. H. Downing, J. Lepault, and F. Zemlin. 1986. Structure of purple membrane from *Halobacterium halobium*: recording, measurement and evaluation of electron micrographs at 3.5 Å resolution. *Ultramicroscopy.* 19:147–178.

Hertzberg, E. L., R. M. Disher, A. A. Tiller, Y. Zhou, and R. G. Cook. 1988. Topology of the Mr 27,000 liver gap junction protein cytoplasmic localization of the amino- and carboxyl termini and a hydrophilic domain which is protease hypersensitive. *J. Biol. Chem.* 265:2138–2147.

Hessler, D., S. J. Young, B. O. Carragher, M. E. Martone, S. Lamont, M. Whittaker, R. A. Milligan, E. Masliah, J. Hinshaw, and M. H. Ellisman. 1992. Programs for visualization in three-dimensional microscopy. *Neuroimage.* 1:55–67.

Hoh, J. H., R. Lal, S. A. John, J.-P. Revel, and M. F. Arnsdorf. 1991. Atomic force microscopy and dissection of gap junctions. *Science.* 235:1405–1408.

Hoh, J., G. E. Sosinsky, J.-P. Revel, and P. K. Hansma. 1993. Structure of the extracellular surface of the gap junction by atomic force microscopy. *Biophys. J.* 65:149–163.

Hooper, M. L., and J. H. Subak-Sharpe. 1981. Metabolic cooperation between cells. *Int. Rev. Cytol.* 69:45–104.

Hurtley, S. M., and A. Helenius. 1989. Protein oligomerization in the endoplasmic reticulum. *Annu. Rev. Cell Biol.* 5:277–307.

Jiang, J. X., and D. A. Goodenough. 1996. Heteromeric connexons in lens gap junction channels. *Proc. Natl. Acad. Sci.* 3:1287–1291.

Karlsson, B., S. Hovmoller, H. Weiss, and K. Leonard. 1983. Structural studies of cytochrome reductase: subunit topography determined by electron microscopy of membrane crystals of a subcomplex. *J. Mol. Biol.* 165:287–302.

Karrasch, S., D. Typke, T. Walz, M. Miller, G. Tsiotis, and A. Engel. 1996. Highly ordered two-dimensional crystals of photosystem I reaction center from *Synechococcus* sp.: functional and structural analyses. *J. Mol. Biol.* 262:336–348.

Laird, D. W. 1996. The life cycle of a connexin: Gap junction formation, removal, and degradation. *J. Bioenerg. Biomembr.* 28:311–318.

Makowski, L. 1988. X-Ray diffraction studies of gap junction structure. *Adv. Cell Biol.* 2:119–158.

Makowski, L., D. L. D. Caspar, W. C. Phillips, T. S. Baker, and D. A. Goodenough. 1984. Gap junctions structures VI. Variation and conservation in connexon conformation and packing. *Biophys. J.* 45:208–218.

Makowski, L., D. L. D. Caspar, W. C. Phillips, and D. A. Goodenough. 1977. Gap junction structure II. Analysis of the X-ray diffraction data. *J. Cell Biol.* 74:629–645.

Manjunath, C. K., G. E. Going, and E. Page. 1984. Detergent sensitivity and splitting of isolated liver gap junctions. *J. Membr. Biol.* 78:147–155.

Meyer, R. A., D. W. Laird, J.-P. Revel, and R. G. Johnson. 1992. Inhibition of gap junction and adherens junction assembly and connexin and N-CAM antibodies. *J. Cell Biol.* 119:179–189.

Milks, L. C., N. M. Kumar, R. Houghten, N. Unwin, and N. B. Gilula. 1988. Topology of the 32-kd liver gap junction protein determined by site-directed antibody localizations. *EMBO J.* 7:2967–2975.

Musil, L. M., and D. A. Goodenough. 1991. Biochemical analysis of connexin43 intracellular transport, phosphorylation, and assembly into gap junctional plaques. *J. Cell Biol.* 115:1357–1374.

Musil, L. M., and D. A. Goodenough. 1993. Multisubunit assembly of an integral plasma membrane channel protein, gap junction connexin43, occurs after exit from the ER. *Cell.* 74:1065–1077.

Nicholson, B. J., D. B. Gros, S. B. H. Kent, L. E. Hood, and J.-P. Revel. 1985. The Mr 28,000 gap junction proteins from rat heart and liver are different but related. *J. Biol. Chem.* 260:6514–6517.

Paul, D. L., L. Ebihara, L. J. Takemoto, K. I. Swenson, and D. A. Goodenough. 1991. Connexin46, a novel lens gap junction protein, induces voltage-gated currents in nonjunctional plasma membrane of Xenopus oocytes. *J. Cell Biol.* 115:1077–1089.

Rachel, R., U. Jakubowski, R. Tietz, R. Hegerl, and W. Baumeister. 1986. Projected structure of the surface protein of Deinococcus radiodurans determined to 8 Å resolution by cryomicroscopy. *Ultramicroscopy.* 20:305–316.

Revel, J.-P., B. J. Nicholson, and S. B. Yancy. 1985. Chemistry of gap junctions. *Annu. Rev. Physiol.* 47:263–279.

Schmid, M., R. Dargahi, and M. Tam. 1993. SPECTRA: A system for processing electron images of crystals. *Ultramicroscopy.* 48:251–264.

Shaw, P. J., and G. J. Hills. 1981. Tilted specimen in the electron microscope: a simple specimen holder and the calculation of tilt angles for crystalline specimens. *Micron.* 12:279–281.

Sikerwar, S. S., K. H. Downing, and R. M. Glaeser. 1991. Three-dimensional structure of an invertebrate intercellular communicating junction. *J. Struct. Biol.* 106:255–263.

Sikerwar, S. S., and N. Unwin. 1988. Three-dimensional structure of gap junctions in fragmented plasma membranes from rat liver. *Biophys. J.* 54:113–119.

Sosinsky, G. E. 1992. Image analysis of gap junction structures. *Electr. Microsc. Rev.* 3:59–76.

Sosinsky, G. E. 1995. Mixing of connexins in gap junction membrane channels. *Proc. Natl. Acad. Sci.* 92:9210–9214.

Sosinsky, G. E. 1996. Molecular organization of gap junction membrane channels. *J. Bioenerg. Biomembr.* 28:297–310.

Sosinsky, G. E., J. C. Jesior, D. L. D. Caspar, and D. A. Goodenough. 1988. Gap junction structures VIII. Membrane cross-sections. *Biophys. J.* 53:709–722.

Stauffer, K. A. 1995. The gap junction protein β_1-connexin (connexin32) and β_2-connexin (connexin26) can form heteromeric hemichannels. *J. Biol. Chem.* 270:6768–6772.

Stevens, J. K., L. R. Mills, and J. E. Trogadis, editors. 1994. Three-Dimensional Confocal Microscopy: Volume Investigation of Biological Systems. Academic Press, San Diego.

Tibbitts, T. T., D. L. D. Caspar, W. C. Phillips, and D. A. Goodenough. 1990. Diffraction diagnosis of protein folding in gap junction connexons. *Biophys. J.* 57:1025–1036.

Unger, V. M., and G. F. X. Schertler. 1995. Low resolution structure of bovine rhodopsin determined by electron cryo-microscopy. *Biophys. J.* 68:1776–1786.

Unwin, N. 1986. Is there a common design for cell membrane channels? *Nature.* 323:12–13.

Unwin, P. N. T., and P. D. Ennis. 1984. Two configurations of a channel-forming membrane protein. *Nature.* 307:609–613.

Unwin, P. N. T., and A. Klug. 1974. Electron microscopy of stacked disk aggregate of tobacco mosaic virus protein II. The influence of electron irradiation on the stain distribution. *J. Mol. Biol.* 262:336–348.

Unwin, P. N. T., and G. Zampighi. 1980. Structure of the junction between communicating cells. *Nature.* 283:545–549.

Valpuesta, J. M., R. Henderson, and T. G. Frey. 1990. Electron cryo-microscopic analysis of crystalline cytochrome oxidase. *J. Mol. Biol.* 214:237–251.

White, T. W., R. Bruzzone, S. Wolfram, D. L. Paul, and D. A. Goodenough. 1994. Selective interactions among multiple connexin proteins expressed in the vertebrate lens: the second extracellular domain is a determinant of compatibility between connexins. *J. Cell Biol.* 125: 879–892.

White, T., D. Paul, D. A. Goodenough, and R. Bruzzone. 1995. Functional analysis of selective interactions among rodent connexins. *Mol. Biol. Cell.* 6:459–70.

Yancy, S. B., S. A. John, R. Lal, B. J. Austin, and J.-P. Revel. 1989. The 43-kD polypeptide of heart gap junctions: immunolocalization, topology, and functional domains. *J. Cell Biol.* 108:2241–2254.

Yeager, M., and N. B. Gilula. 1992. Membrane topology and quaternary structure of cardiac gap junction ion channels. *J. Mol. Biol.* 223: 929–948.

Zhang, J.-T., and B. J. Nicholson. 1989. Sequence and tissue distribution of a second protein of hepatic gap junctions, Cx26, as deduced from its cDNA. *J. Cell Biol.* 109:3391–3401.

Zimmer, D. B., C. R. Green, W. H. Evans, and N. B. Gilula 1987. Topological analysis of the major protein in isolated intact rat liver gap junctions and gap junction-derived single membrane structures. *J. Biol. Chem.* 262:7751–7763.